

A Hybrid Atmospheric Model Incorporating Machine Learning Can Capture Dynamical Processes Not Captured by Its Physics-Based Component

Troy Arcomano^{1,2}, Istvan Szunyogh¹, Alexander Wikner³, Brian R Hunt^{2,4}, and Edward Ott^{3,4}

¹Department of Atmospheric Sciences, Texas A&M University

²Institute for Physical Science and Technology, University of Maryland

³Department of Physics, University of Maryland

⁴Department of Electrical and Computer Engineering, University of Maryland

December 27, 2022

1 **A Hybrid Atmospheric Model Incorporating Machine**
2 **Learning Can Capture Dynamical Processes Not**
3 **Captured by Its Physics-Based Component**

4 **Troy Arcomano^{1*}, Istvan Szunyogh¹, Alexander Wikner², Brian R. Hunt³, and**
5 **Edward Ott^{2,4}**

6 ¹Department of Atmospheric Sciences, Texas A&M University, College Station, TX, USA

7 ²Department of Physics, University of Maryland, College Park, MD, USA

8 ³Institute for Physical Science and Technology, University of Maryland, College Park, MD, USA

9 ⁴Department of Electrical and Computer Engineering, University of Maryland, College Park, MD, USA

10 **Key Points:**

- 11 • A hybrid system combining an AGCM with a machine-learning component can
12 capture processes not captured by the AGCM.
- 13 • Machine learning provides a flexible framework to introduce additional prognos-
14 tic variables into the hybrid model.
- 15 • The prototype hybrid model tested in the paper is stable and has a realistic cli-
16 mate in decades-long simulation experiments.

*Current address, Argonne National Laboratory

Corresponding author: Troy Arcomano, tarcomano@anl.gov

17 **Abstract**

18 It is shown that a recently developed hybrid modeling approach that combines machine
 19 learning (ML) with an atmospheric global circulation model (AGCM) can serve as a ba-
 20 sis for capturing atmospheric processes not captured by the AGCM. This power of the
 21 approach is illustrated by three examples from a decades-long climate simulation exper-
 22 iment. The first example demonstrates that the hybrid model can produce sudden strato-
 23 spheric warming (SSW), a dynamical process of nature not resolved by the low resolu-
 24 tion AGCM component of the hybrid model. The second and third example show that
 25 introducing 6-h cumulative precipitation and sea surface temperature (SST) as ML-based
 26 prognostic variables improves the precipitation climatology and leads to a realistic ENSO
 27 signal in the SST and atmospheric surface pressure.

28 **Plain Language Summary**

29 This paper introduces and tests schemes for efficiently enabling significant expansion
 30 of the utility and scope of a recently introduced hybrid modeling technique that com-
 31 bines machine learning with an atmospheric global circulation model (AGCM). Simu-
 32 lation experiments are carried out with an implementation of the approach on a low res-
 33 olution simplified AGCM. An examination of the simulated atmospheric circulation sug-
 34 gests that the hybrid model can capture dynamical process not captured by the AGCM.
 35 Moreover, the addition of precipitation and sea surface temperature as machine learn-
 36 ing predicted physical quantities to the model improves the precipitation climatology and
 37 leads to a realistic El Niño-La Niña signal in the SST and atmospheric surface pressure.

38 **1 Introduction**

39 Arcomano et al. (2022) (AEA22 hereafter) described a hybrid atmospheric mod-
 40 eling approach that combines machine learning (ML) with an atmospheric general cir-
 41 culation model (AGCM). They showed that, when the hybrid model was used for weather
 42 prediction, it provided more accurate short and medium range (1-7 days) forecasts than
 43 either the AGCM or the ML-only component of the model (Arcomano et al., 2020) act-
 44 ing alone. They also showed that when the model was used for climate simulations, it
 45 greatly reduced the systematic errors (biases) of the model climate compared to that of
 46 the AGCM. In the present study, we further explore the potential of the approach of AEA22
 47 for climate modeling, and describe methods that significantly extends its utility and scope.
 48 The results we report are in accord with the idea that the inaccuracies of an AGCM could
 49 potentially be mitigated by utilization of information in time series of past observational
 50 data via the ML component of the hybrid.

51 The approach of AEA22 is an implementation of the combined hybrid/parallel pre-
 52 diction (CHyPP) scheme of Wikner et al. (2020) on an AGCM. CHyPP itself is an adap-
 53 tation of the hybrid modeling approach of Pathak, Wikner, et al. (2018) to large dynam-
 54 ical systems, using the parallel reservoir computing (RC) algorithm of Pathak, Hunt, et
 55 al. (2018) for ML. Other hybrid approaches recently proposed for earth system model-
 56 ing (Brenowitz & Bretherton, 2018, 2019; Rasp et al., 2018; Chattopadhyay et al., 2020;
 57 Farchi et al., 2021; Gentine et al., 2018; Watt-Meyer et al., 2021; Clark et al., 2022) use
 58 either random forests or deep learning for ML.

59 Section 2 summarizes the approach of AEA22 and explains how additional prog-
 60 nostic variables can be introduced into the hybrid model without changing the AGCM.
 61 Section 3 demonstrates the potential of the approach by three examples from a climate
 62 simulation experiment. The first example, the presence of sudden stratospheric warm-
 63 ing (SSW) events, illustrates that the hybrid model can capture some dynamical pro-
 64 cesses of nature not resolved by the AGCM. The second and third example, realistic pre-
 65 cipitation climatology and SST variability, demonstrate that some other dynamical pro-

66 cesses can be reproduced by modifying the AEA22 hybrid via addition of new ML-based
 67 prognostic variables (precipitation and sea surface temperature). As in AEA22, the AGCM
 68 of the simulation experiments is the Simplified Parameterization, primitive-Equation Dy-
 69 namics (SPEEDY) model (Kucharski et al., 2006; Molteni, 2003).

70 2 The Hybrid Modeling Approach

71 2.1 The Hybrid Modeling Approach of AEA22

72 The hybrid model uses the same computational grid as the AGCM. The elements
 73 of the hybrid global state vector $\mathbf{v}_G^H(t)$ and physics-based global state vector $\mathbf{v}_G^P(t)$ are
 74 the grid-point values of the prognostic model variables. The input of the “one-time-step”
 75 hybrid global model solution $\mathbf{v}_G^H(t+\Delta t)$ is $\mathbf{v}_G^H(t)$, where the “time step” Δt is signifi-
 76 cantly longer than the time step of the AGCM. No changes are made to the AGCM, which
 77 is started from $\mathbf{v}_G^H(t)$ to provide the physics-based contribution $\mathbf{v}_G^P(t+\Delta t)$ to $\mathbf{v}_G^H(t+\Delta t)$.
 78 The hybridization is done by subdividing the global atmosphere into L local regions
 79 and obtaining a hybrid local model solution for each region. The computations for the
 80 different local regions ($\ell = 1, 2, \dots, L$) are carried out in parallel and $\mathbf{v}_G^H(t+\Delta t)$ is ob-
 81 tained by assembling the hybrid local solutions. The next paragraph outlines the cal-
 82 culations that provide the hybrid local model solution for local region ℓ .

The elements of the physics based local state vector $\check{\mathbf{v}}_\ell^P(t+\Delta t)$ are the standard-
 ized elements of $\mathbf{v}_G^P(t+\Delta t)$ that fall into local region ℓ . (Hereafter, the symbol $\check{\mathbf{x}}$ in-
 icated a standardized vector obtained by subtracting a related mean value and divid-
 ing by a related standard deviation for each element of \mathbf{x} .) The “one-time-step” hybrid
 local model solution is

$$\check{\mathbf{v}}_\ell^H(t+\Delta t) = \mathbf{W}_\ell \begin{pmatrix} \check{\mathbf{v}}_\ell^P(t+\Delta t) \\ \tilde{\mathbf{r}}_\ell(t+\Delta t) \end{pmatrix}, \quad (1)$$

where \mathbf{W}_ℓ is a weight matrix whose entries are to be determined by ML training, which
 will be discussed in Sec. 2.2. The D_r -dimensional vector $\tilde{\mathbf{r}}_\ell(t+\Delta t)$ is a quadratic func-
 tion of the reservoir state vector $\mathbf{r}_\ell(t+\Delta t)$, where the reservoir is a dynamical system
 with evolution equation (Jaeger, 2001; Lukoševičius & Jaeger, 2009; Lukoševičius, 2012)

$$\mathbf{r}_\ell(t+\Delta t) = \tanh[\mathbf{A}_\ell \mathbf{r}_\ell(t) + \mathbf{B}_\ell \check{\mathbf{u}}_\ell(t)]. \quad (2)$$

83 Each entry of the $D_r \times D_r$ weighted adjacency matrix \mathbf{A}_ℓ is randomly chosen with a
 84 probability κ/D_r of being nonzero and assigned a random value chosen uniformly in $(0, 1]$.
 85 The nonzero entries are scaled such that the magnitude of the largest eigenvalue of \mathbf{A}_ℓ
 86 has a prescribed value ρ ($0 < \rho < 1$), called the spectral radius. The D_u -dimensional
 87 vector $\check{\mathbf{u}}_\ell(t)$ is the input vector of the reservoir, whose elements are standardized elements
 88 of the global hybrid state vector $\mathbf{v}_G^H(t)$ from an extended local region that has overlaps
 89 with its four neighbors. \mathbf{B}_ℓ is a matrix with entries chosen randomly on the interval $(-\alpha, \alpha)$,
 90 where α is an adjustable parameter. The hybrid local model solution is obtained by trans-
 91 forming the standardized values of the elements of $\check{\mathbf{v}}_\ell^H(t+\Delta t)$ to non-standardized val-
 92 ues.

93 The initial value of $\mathbf{v}_G^H(0)$ at the beginning of a forecast or simulation is a conven-
 94 tional observational analysis $\mathbf{v}_G^A(0)$ for the AGCM. Starting the hybrid model also re-
 95 quires an initial value $\mathbf{r}_\ell(0)$ for each of the L reservoir state vectors. These initial val-
 96 ues are obtained using Equation 2 to synchronize the evolution of the reservoirs with the
 97 atmospheric states for a short period prior ($t < 0$) to the start time of the forecast or
 98 simulation. This synchronization is achieved by feeding the reservoirs input vectors based
 99 on observational analyses for the synchronization period.

100

2.2 Training the Hybrid Model

101

102

103

104

105

106

107

The machine-learning component of the model learns to predict $\check{\mathbf{v}}_\ell^H(t+\Delta t)$ from $\mathbf{v}_G^H(t)$ for each local region by training. The training data are based on global observational analyses $\mathbf{v}_G^A(t)$. These analyses provide the initial conditions for the Δt -long AGCM forecasts and are standardized and restricted to the extended local region to form the input $\mathbf{u}_\ell(t)$ for each of the L reservoirs. To promote stability, a small-magnitude random noise $\varepsilon(k\Delta t)$ is introduced into the analyses before forming the input vectors by the formula $[1 + \varepsilon(k\Delta t)]\mathbf{v}_G^A(k\Delta t)$.

The training data after standardization also provide the elements of the desired outcome $\check{\mathbf{v}}_\ell^A(t+\Delta t)$ to which $\check{\mathbf{v}}_\ell^H(t+\Delta t)$ can be compared during training. Formally, the training seeks the weight matrix \mathbf{W}_ℓ for which the ‘‘one-time-step’’ predictions $\check{\mathbf{v}}_\ell^H(k\Delta t, \mathbf{W}_\ell)$ ($k = -K + 1, -K + 2, \dots, 0$) best fit $\check{\mathbf{v}}_\ell^A(k\Delta t)$ in a least-square sense. That is, \mathbf{W}_ℓ is the minimizer of the quadratic cost-function

$$J(\mathbf{W}_\ell) = \sum_{k=-K+1}^0 \|\check{\mathbf{v}}_\ell^H(k\Delta t, \mathbf{W}_\ell) - \check{\mathbf{v}}_\ell^A(k\Delta t)\|^2 + \beta^P \|\mathbf{W}^P\|^2 + \beta^R \|\mathbf{W}^R\|^2, \quad (3)$$

where \mathbf{W}^P and \mathbf{W}^R are matrices for which

$$\check{\mathbf{v}}_\ell^H(t + \Delta t) = \mathbf{W}_\ell^P \check{\mathbf{v}}_\ell^P(t + \Delta t) + \mathbf{W}_\ell^R \tilde{\mathbf{r}}_\ell(t + \Delta t), \quad \mathbf{W}_\ell = \begin{pmatrix} \mathbf{W}_\ell^P & \mathbf{W}_\ell^R \end{pmatrix}, \quad (4)$$

108

109

110

is equivalent to Equation 1. The adjustable parameters β^P and β^R are chosen regularization parameters (Tikhonov and Arsenin 1977). It can be shown that the direct solution of the minimization problem is the matrix

$$\mathbf{W}_\ell = \begin{pmatrix} \mathbf{V}_\ell^A (\mathbf{V}_\ell^P)^T & \mathbf{V}_\ell^A \tilde{\mathbf{R}}_\ell^T \end{pmatrix} \begin{pmatrix} \mathbf{V}_\ell^P (\mathbf{V}_\ell^P)^T + \beta^P \mathbf{I} & \mathbf{V}_\ell^P \tilde{\mathbf{R}}_\ell^T \\ \tilde{\mathbf{R}}_\ell (\mathbf{V}_\ell^P)^T & \tilde{\mathbf{R}}_\ell \tilde{\mathbf{R}}_\ell^T + \beta^R \mathbf{I} \end{pmatrix}^{-1}. \quad (5)$$

111

112

113

In this equation, column k of the matrix \mathbf{V}_ℓ^P is the local state vector $\check{\mathbf{v}}_\ell^P(k\Delta t)$ that corresponds to the physics-based model solution $\mathbf{v}_G^P(k\Delta t)$ started from $\mathbf{v}_G^A[(k-1)\Delta t]$, column k of the matrix $\tilde{\mathbf{R}}_\ell$ is $\tilde{\mathbf{r}}_\ell(k\Delta t)$, and column k of the matrix \mathbf{V}_ℓ^A is $\check{\mathbf{v}}_\ell^A(k\Delta t)$.

114

2.3 Introducing New ML-Based Prognostic Variables

115

116

117

118

119

120

121

122

123

In atmospheric modeling, the term ‘prognostic variable’ refers to a state variable whose temporal evolution is predicted directly by a model equation. The hybrid approach provides a framework for introducing new prognostic variables without making any changes to the AGCM provided that training data are available for the new variables. Two specific methods that take advantage of this flexibility are described here: Method I is designed for atmospheric variables that are not required to evolve the AGCM; while Method II is designed for external variables, variables represented by prescribed boundary fields in a standalone AGCM, which might vary on a different time scale than the atmospheric prognostic variables.

124

2.3.1 Method I

125

126

127

128

The purpose of Method I is to introduce a prognostic variable that is either not predicted by the AGCM, or predicted only indirectly as a ‘byproduct’ of the parameterization schemes. This approach will be demonstrated by introducing precipitation as a prognostic variable (Section 3).

Let

$$\mathbf{v}_G^{H+}(t + \Delta t) = \begin{pmatrix} \mathbf{v}_G^H(t + \Delta t) \\ \mathbf{v}_G^{H*}(t + \Delta t) \end{pmatrix} \quad (6)$$

be the global state vector of hybrid model, where $\mathbf{v}_G^{H*}(t)$ represents the global field of a new prognostic variable. The corresponding local state vector for local region ℓ is

$$\check{\mathbf{v}}_\ell^{H+}(t + \Delta t) = \begin{pmatrix} \check{\mathbf{v}}_\ell^H(t + \Delta t) \\ \check{\mathbf{v}}_\ell^{H*}(t + \Delta t) \end{pmatrix}. \quad (7)$$

The equation of the reservoir dynamics is modified as

$$\mathbf{r}_\ell^+(t + \Delta t) = \tanh [\mathbf{A}_\ell \mathbf{r}_\ell^+(t) + \mathbf{B}_\ell \check{\mathbf{u}}_\ell^+(t)], \quad (8)$$

where $\check{\mathbf{u}}_\ell^+(t)$ is an extended local state vector, which also includes the grid-point values of the new prognostic variable from the extended local region. In addition, Equation 4 is modified as

$$\check{\mathbf{v}}_\ell^{H+}(t + \Delta t) = \begin{pmatrix} \check{\mathbf{v}}_\ell^H(t + \Delta t) \\ \check{\mathbf{v}}_\ell^{H*}(t + \Delta t) \end{pmatrix} = \begin{pmatrix} \mathbf{W}_\ell^P \\ \mathbf{W}_\ell^{P*} \end{pmatrix} \check{\mathbf{v}}_\ell^P(t + \Delta t) + \begin{pmatrix} \mathbf{W}_\ell^R \\ \mathbf{W}_\ell^{R*} \end{pmatrix} \tilde{\mathbf{r}}_\ell^+(t + \Delta t)$$

129 which leads to the following modification of Equation 1:

$$\begin{aligned} \check{\mathbf{v}}_\ell^{H+}(t + \Delta t) &= \begin{pmatrix} \check{\mathbf{v}}_\ell^{H+}(t + \Delta t) \\ \check{\mathbf{v}}_\ell^{H*}(t + \Delta t) \end{pmatrix} = \mathbf{W}_\ell \begin{pmatrix} \check{\mathbf{v}}_\ell^P(t + \Delta t) \\ \tilde{\mathbf{r}}_\ell^+(t + \Delta t) \end{pmatrix} \\ \mathbf{W}_\ell &= \begin{pmatrix} \mathbf{W}_\ell^P & \mathbf{W}_\ell^R \\ \mathbf{W}_\ell^{P*} & \mathbf{W}_\ell^{R*} \end{pmatrix}. \end{aligned} \quad (9)$$

130 2.3.2 Method II

131 In an AGCM, the effects of the other earth system components, such as the ocean,
 132 cryosphere, land, and biosphere on the atmosphere are taken into account by param-
 133 eterization schemes that include fields of some state variables of the other components
 134 at the earth's surface as input. In a standalone AGCM these fields must be prescribed.
 135 For instance, the thermal effects of the ocean on the atmosphere are taken into account
 136 by schemes that include prescribed SST fields, which are based on past SST observational
 137 analyses in the case of a climate simulation, or the latest SST analysis in the case of a
 138 weather forecast. A limitation of this approach is that it does not take into account feed-
 139 backs from the state variables of the AGCM to the prescribed state variables. Method II
 140 addresses this issue by replacing a prescribed field with an ML-based prognostic vari-
 141 able. It also takes into account the fact that the climate-relevant effects of these feed-
 142 backs on the atmosphere typically occur on time scales that are different than the time
 143 scale of the changes of the atmosphere on which the AGCM evolves. Method II will be
 144 demonstrated by introducing SST as a prognostic variable (Section 3).

In contrast with Method I, the reservoirs for the new prognostic variable are separate from the original reservoirs of the hybrid model. Let $\mathbf{v}_G^{H*}(t)$ be the state vector that represents the global state of the new variable in the hybrid model, and $\check{\mathbf{v}}_\ell^{H*}(t)$ ($\ell = 1, 2, \dots, L$) the related local state vectors. The ML-based ‘‘prognostic equation’’ for local vectors ℓ is

$$\check{\mathbf{v}}_\ell^{H*}(t + \Delta t^*) = \mathbf{W}_\ell^{R*} \tilde{\mathbf{r}}_\ell^*(t + \Delta t^*), \quad (10)$$

where

$$\mathbf{r}_\ell^*(t + \Delta t^*) = \tanh [\mathbf{A}_\ell^* \mathbf{r}_\ell^*(t) + \mathbf{B}_\ell^* \check{\mathbf{u}}_\ell^*(t)]. \quad (11)$$

145 The input vector $\mathbf{u}_\ell^*(t)$ includes standardized grid-point values of both the new variable
 146 and the original variables, while the ‘‘time step’’ Δt^* is not necessarily equal to Δt (an-
 147 other difference with Method I). For instance, when the newly added prognostic vari-
 148 able evolves on a slower time scale than the atmospheric prognostic variable (e.g., the
 149 SST), $\Delta t^* > \Delta t$, and the interactions between the new variable and the atmospheric
 150 variables are treated as follows: (1) the time $t + n\Delta t$ ($n = 1, 2, \dots, \Delta t^*/\Delta t - 1$) input
 151 from the new prognostic variable to the AGCM and the atmospheric reservoirs are the
 152 values at time t ; and (2) the time t input from the atmospheric prognostic variables to

153 the reservoirs of the new prognostic variable are the average values for the “time steps”
 154 $t + n\Delta t$ ($n = 0, 1, \dots, \Delta t^*/\Delta t$).

The weight matrix \mathbf{W}_ℓ^{R*} is computed separately from \mathbf{W}_ℓ^R by

$$\mathbf{W}_\ell^{R*} = \mathbf{V}_\ell^{A*} \tilde{\mathbf{R}}_\ell^{*T} \left(\tilde{\mathbf{R}}_\ell^* \tilde{\mathbf{R}}_\ell^{*T} + \beta^{R*} \mathbf{I} \right)^{-1}, \quad (12)$$

155 where β^{R*} is a regularization parameter, column k of the matrix $\tilde{\mathbf{R}}_\ell^*$ is $\tilde{\mathbf{r}}_\ell^*(k\Delta t^*)$, and
 156 column k of the matrix \mathbf{V}_ℓ^{A*} is $\check{\mathbf{v}}_\ell^{A*}(k\Delta t^*)$ (the local vector of training data for time $k\Delta t$).

157 3 Climate Simulation Experiment

158 3.1 Experiment Design

159 The hybrid model is the same as in AEA22, except that precipitation and SST are
 160 added as prognostic variables to the two horizontal coordinates of the wind vector, tem-
 161 perature, specific humidity, and the logarithm of the surface pressure. The precipitation
 162 variable is defined by $\ln(P/0.001 + 1)$, where P is the cumulative precipitation for the
 163 prior 6 h. The fields of the SST, precipitation, and logarithm of the surface pressure are
 164 two-dimensional, while the fields of the other variables are three-dimensional. All fields
 165 are represented by a $3.75^\circ \times 3.75^\circ$ horizontal grid, while the three-dimensional fields have
 166 eight vertical levels at sigma equals 0.95, 0.835, 0.685, 0.51, 0.34, 0.20, 0.095, and 0.025.
 167 The $L = 1, 152$ local regions for the atmospheric state variables have a $7.5^\circ \times 7.5^\circ$ hor-
 168 izontal footprint and contain all vertical levels. The extended local regions have a hor-
 169 izontal footprint of $15.0^\circ \times 15.0^\circ$ with an overlap of 3.75° (1 grid point) on each side.
 170 The climatological mean and standard deviation for the standardization of the compo-
 171 nents of the local state vectors and input vectors of the reservoirs are computed for the
 172 specific variable at the specific vertical level for the extended local region.

173 The input vectors of the reservoirs for the atmospheric prognostic variables include
 174 the standardized values of the atmospheric prognostic variables from the extended lo-
 175 cal region, plus the incoming solar radiation at the top of the atmosphere. The “time
 176 step” for the atmospheric state variables is $\Delta t = 6$ h. The other hyper-parameters of
 177 the reservoirs for the atmospheric prognostic variables are $D_r = 6000$, $\alpha = 0.5$, $\beta^R =$
 178 10^{-4} , $\beta^P = 1$, $\kappa = 6$, $\varepsilon = 0.2$, ρ increases from 0.3 at the equator to 0.7 at latitude
 179 45° and beyond. A local state vector and reservoir are created for the SST only if the
 180 local region includes at least one oceanic grid point. The coordinates of the local state
 181 vectors are the standardized SST values at the oceanic grid points. (A similar approach
 182 is employed in the standalone parallel RC-based global SST model of Walleshauser and
 183 Bollt (2022)). The “time step” for the SST is $\Delta t^* = 168$ h (7 days), which is 28 times
 184 longer than Δt . The elements of the input vectors of the reservoirs are the averages of
 185 the atmospheric state variables at the lowest model level for the period $[t, t + \Delta t^*]$ and
 186 the SST at time t from the extended local region. At grid points over land, the SST el-
 187 ements of the input vectors are set to a predefined constant (land mask) value. A non-
 188 standardized SST value $\leq -1^\circ\text{C}$ is assumed to indicate ice. In a local region where the
 189 ocean is permanently covered by ice in the training data, the ocean is assumed to remain
 190 covered by ice. In a local region where both water and ice are present in the training data,
 191 the phase of sea water is allowed to change, but non-standardized values of the SST that
 192 are $< -1^\circ\text{C}$ at the end of a time step are reset to -1°C . The other hyperparameters
 193 for the SST are $D_r^* = 4000$, $\alpha^* = 0.6$, $\beta^{R*} = 10^{-4}$, $\kappa^* = 6$, $\rho^* = 0.9$, $\varepsilon^* = 0.1$. The
 194 feedback from the SST to the atmosphere is introduced by replacing the prescribed SST
 195 field of SPEEDY with the last predicted values of the SST, which stays constant for 7
 196 days.

197 The training and verification data are ERA5 reanalyses (Hersbach et al., 2020). The
 198 training period is from 0000UTC 1 January 1981 to 0000UTC 1 December 2006. The
 199 ERA5 reanalyses from December 2006 are used to keep the reservoirs synchronized with

200 the atmosphere, and a 70-year simulation experiment (free run without observational in-
 201 put) is started from the ERA5 reanalysis for 0000 UTC 1 January 2007. The hybrid model
 202 remains stable and produces a realistic climate for the entirety of the experiment. The
 203 hybrid model climatology for the first 40 years of this experiment is compared to the ERA5
 204 climatology for 1981-2020, and the 40-year climatology for a free run with SPEEDY, which
 205 is also started from the ERA5 reanalysis for 000UTC 1 January 2007. The prescribed
 206 SST field for SPEEDY is the daily varying 40-year ERA5 SST climatology.

207 **3.2 Sudden Stratospheric Warming**

208 The dominant features of stratospheric variability are wintertime events of sudden
 209 stratospheric warming (SSW) in the NH. The term SSW refers to a dynamical process
 210 in which the normally strong westerly zonal mean flow at the edge of the NH stratospheric
 211 polar vortex suddenly turns easterly, which leads to a sudden rise of the polar strato-
 212 spheric temperature. This rapid change is caused by an unusually strong coupling be-
 213 tween the dynamics of the stratospheric and tropospheric flow (Andrews et al., 1987).
 214 While SPEEDY would need additional vertical levels above 25 hPa (its current top level)
 215 to produce realistic stratospheric dynamics, the hybrid model can produce realistic SSW
 216 events (Figure 1). The blue curves and gray shades show, respectively, the calendar-day
 217 mean and year-to-year variability of the strength of the zonal flow at the edge of the strato-
 218 spheric polar vortex (top three panels) and the polar temperature (bottom three pan-
 219 els). From July to December, the stratospheric flow (left panels) first turns from east-
 220 erly (negative values) to westerly (positive values), and then it gradually strengthens un-
 221 til midwinter, when it starts to weaken and eventually turns easterly again in April. The
 222 mean polar temperature gradually decreases from midsummer to midwinter, when it starts
 223 to increase to complete the cycle. The variability of the strength of the zonal flow and
 224 the polar temperature is low from May to September and high from October to April,
 225 with a maximum in midwinter. While both the hybrid model (middle two panels) and
 226 SPEEDY (right two panels) can capture the mean trends, the hybrid model somewhat
 227 overestimates, while SPEEDY substantially underestimates the variability of the flow.
 228 The relationship between the variability of the flow and SSW can be further investigated
 229 by using the criteria of Charlton and Polvani (2007) to detect SSW: an event occurs when
 230 the stratospheric zonal mean of the zonal wind at 60°N turns easterly and then it turns
 231 back to westerly for at least 10 consecutive days. Here, the criteria is applied to the zonal
 232 wind at vertical pressure level 25 hPa. For ERA5, the hybrid model, and SPEEDY, there
 233 are 0.6, 0.87, and zero SSW events per year, respectively. The examples for an event shown
 234 by the red curves in Fig. 1 illustrate that both the speed of the onset and the duration
 235 of the SSW are captured realistically by the hybrid model.

236 **3.3 Precipitation Climatology**

237 The prognostic precipitation variable of the hybrid model provides cumulative pre-
 238 cipitation values with 6 hourly resolution, while the diagnostic precipitation variable of
 239 SPEEDY provides this variable with a monthly resolution. The precipitation model cli-
 240 matologies of Figure 2 are based on these variables. This figure shows that the hybrid
 241 model produces lower magnitude precipitation biases than SPEEDY at most locations
 242 (top two rows of panels): the 1.29 mm per day global root-mean-square of the bias for
 243 SPEEDY is reduced to 0.63 mm per day for the hybrid model, and the absolute value
 244 of the largest-magnitude local bias is reduced from 10.50 mm per day to 5.17 mm per
 245 day. SPEEDY has a dry bias in the extension regions of the Kuroshio Current and Gulf
 246 Stream (two right panels), which is greatly reduced by the hybrid approach (top two mid-
 247 dle panels). The bias is also lower for the hybrid model than SPEEDY in mountainous
 248 regions (e.g., Rockies, Himalayas) and equatorial South America and Africa. One region
 249 where the hybrid model has a larger bias than SPEEDY is the Tropical Pacific, where

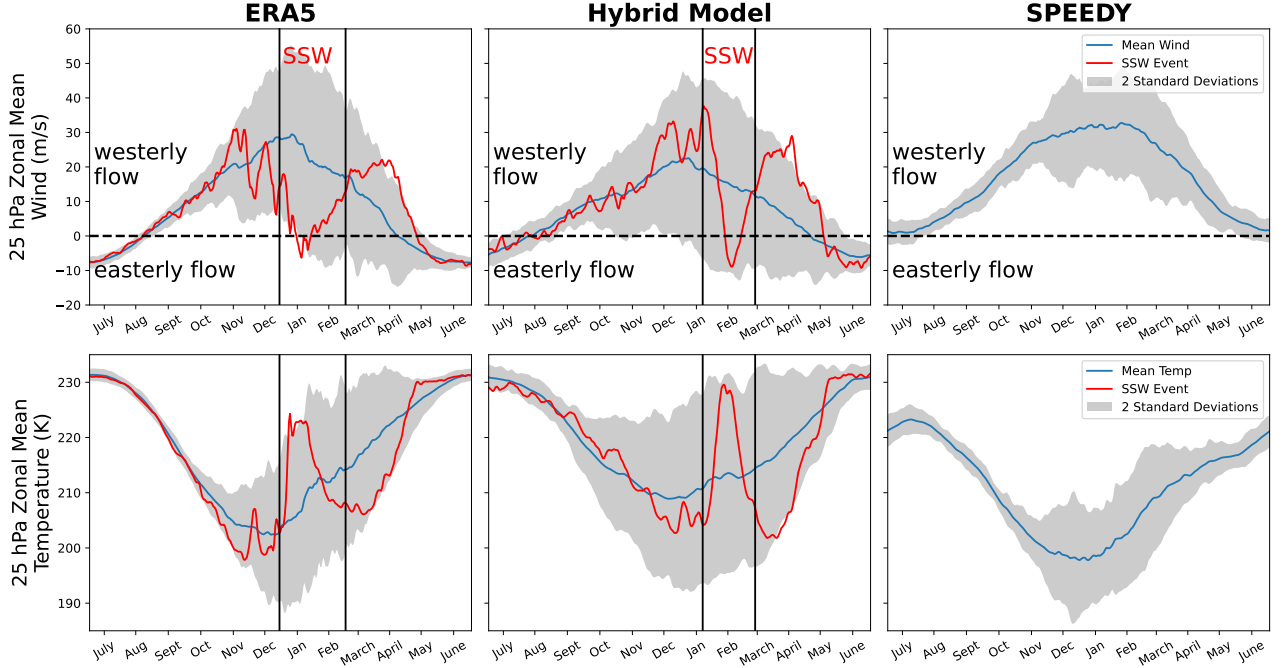


Figure 1. The performance of the hybrid model in capturing SSW. Results are shown for the (left) ERA5 reanalyses, (center) hybrid model, and (right) SPEEDY. Results are shown at the 25 hPa pressure level for (top panels) the mean of the zonal wind component in the 55°N-65°N latitude band, and (bottom panels) the mean temperature north of 60°N. Blue curves show the climatological daily mean, while the gray shading characterizes the annual variability by displaying the range between plus and minus two standard deviations. Positive values of the wind indicate westerly flow, while negative values indicate easterly flow. The red curves show the same diagnostics as the blue curves, except for a particular SSW event rather than the 40-year mean. (No SSW event is detected for SPEEDY.) The event from ERA5 took place in 2013.

250 it has a wet bias. Interestingly, the hybrid model produces a “double ITCZ”, which has
 251 also been a persistent problem for physics-based models (Zhang et al., 2019).

252 In addition to providing improved mean precipitation, the hybrid model produces
 253 precipitation events of varying intensity at the correct rates in the range from about 1 mm/6 h
 254 to about 7-8 mm/6 h, and it only slightly underestimates the frequency of low and ex-
 255 treme high intensity precipitation (bottom panel).

256 3.4 SST Climatology and ENSO

257 The SST prognostic variable (Fig. 3, left panels) has low biases: the global root-
 258 mean-square value of the SST bias is 0.43°C, while the largest local values of the bias
 259 are in the 1°-2°C range. While the model correctly captures the main regions of largest
 260 temporal variability of the SST (Fig. 3, right panels), it tends to somewhat underesti-
 261 mate the variability associated with the western boundary currents and their extension
 262 regions, and overestimate the variability associated with ENSO in the Equatorial Pa-
 263 cific near the coast of South America.

264 The skills and the limitations of the model in capturing climate variability related
 265 to ENSO are further illustrated by Fig. 4. Two of the most common metrics used for di-

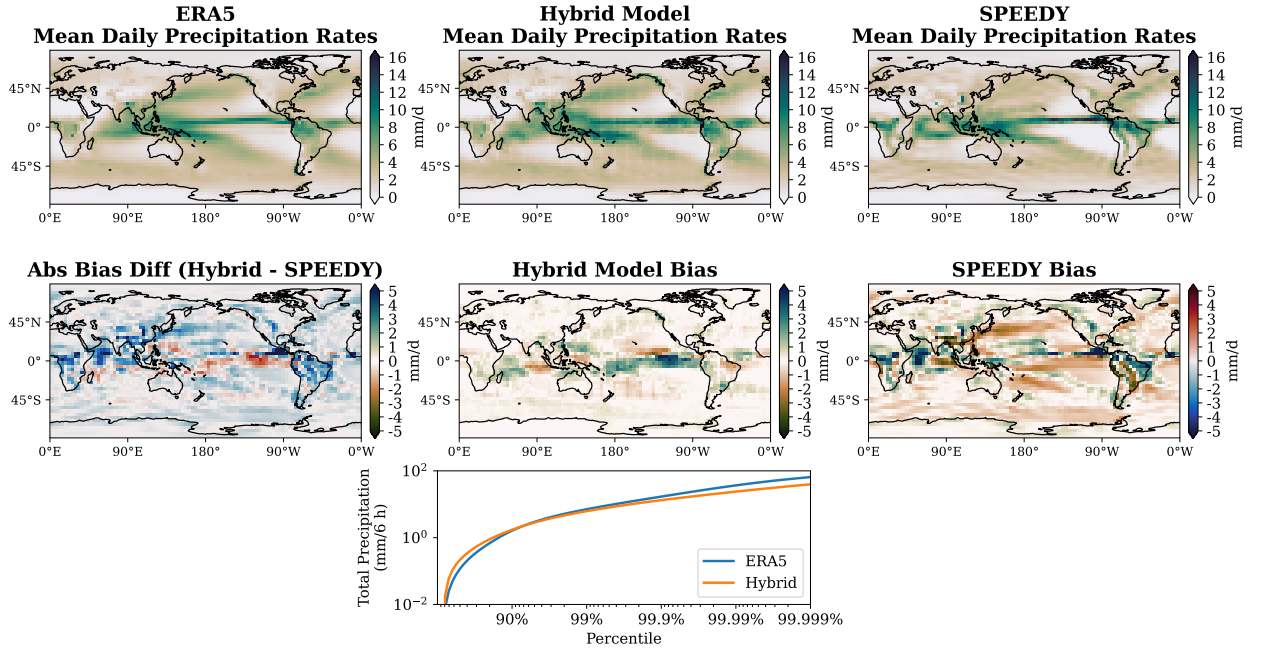


Figure 2. The performance of the hybrid model in capturing the precipitation climatology. Shown is the climatological daily mean precipitation rate for (top left) ERA5, (top center) the hybrid model, and (top right) SPEEDY. Also shown are (middle left) the difference between the biases of the daily precipitation rates for the hybrid model and SPEEDY, and (middle center) the biases of the daily precipitation rates for the hybrid model and (middle right) SPEEDY. Also shown (bottom center) are the rates of occurrence of different precipitation intensities in percentile for (blue) ERA5 and (orange) the hybrid model.

266 agnosing ENSO phases are the Oceanic Niño Index (ONI) and the Southern Oscillation
 267 Index (SOI) for the Niño 3.4 region (5°S - 5°N , 120°W - 170°W). The model correctly cap-
 268 tures the inverse relationship between the smoothed time series of the two indexes (top
 269 panel). In addition, the autocorrelation function of the Niño 3.4 SST anomalies for the
 270 model is in good agreement with that for the ERA5 reanalyses for the first 6 months of
 271 lag (bottom left panel). The model, however, does not capture the timing of the crossover
 272 into negative autocorrelation at about 10 months: the model transitions from one phase
 273 of ENSO to another with a delay. In addition, the occurrence of ENSO is more regular
 274 in the model than in the reanalyses, with too much power at period 5 years, and too lit-
 275 tle power at period 3, 4, and 7 years (bottom right panel). While some climate models
 276 produce too much variability associated with ENSO in the western Tropical Pacific (Menary
 277 et al., 2018), the hybrid model does not exhibit such behavior (Fig. 3, bottom right panel).

278 4 Conclusions

279 The goal of this paper was to demonstrate that hybridizing an AGCM by incor-
 280 porating ML can help the model to capture dynamical processes of nature that are miss-
 281 ing from climate simulations with the AGCM. For some dynamical processes, this po-
 282 tential can be realized without introducing new prognostic variables in the ML compo-
 283 nent of the model. This point was illustrated with the process of SSW. Some other pro-
 284 cesses can be introduced into the model dynamics by adding new ML-based prognostic

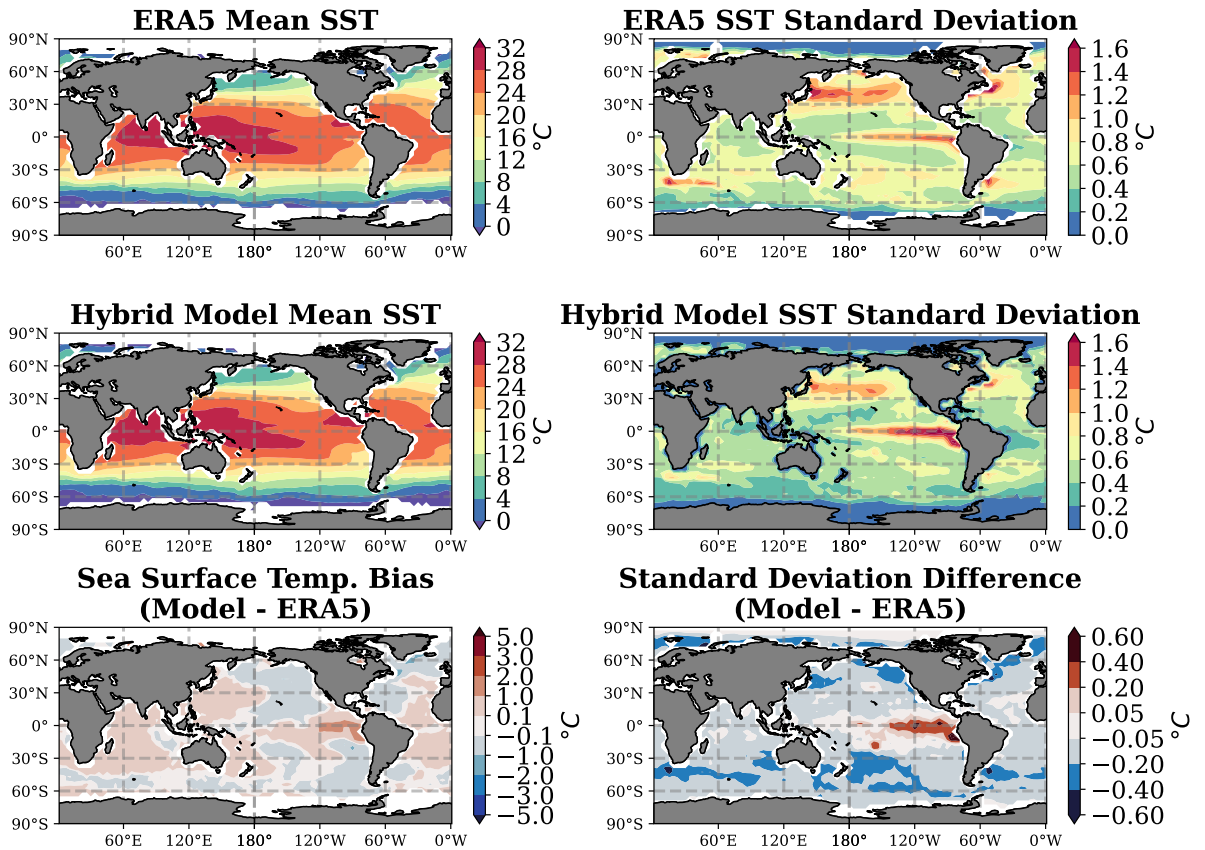


Figure 3. The SST climatology of the hybrid model. Shown are the climatological mean SST for (top left) ERA5, (middle left) the hybrid model, and (bottom left) the difference between the two fields; and the standard deviation of the monthly mean SST for (top right) ERA5 and (middle right) the hybrid model, and (bottom right) the difference between the two fields.

285 variables. This point was illustrated by two examples. First, the 6-h cumulative precip-
 286 itation was introduced as a prognostic variable, and it was shown that the model pro-
 287 duced a highly realistic climatology for the newly added prognostic variable. Second, SST,
 288 which is a prescribed boundary parameter of the AGCM, was turned into a prognostic
 289 variable. The SST prognostic variable had highly realistic climatology, and it also had
 290 a realistic ENSO signal. Moreover, the hybrid model also correctly captured the related
 291 atmospheric surface pressure signal, the indication of a realistic two-way coupling be-
 292 tween an oceanic state variable and the model atmosphere. We conjecture that similar
 293 two-way coupling could be introduced for other interacting components of the earth sys-
 294 tem by turning other boundary parameters into prognostic variables.

295 The one important caveat concerning our conclusions is that they are based on the
 296 application of the hybrid approach to an AGCM that has much lower resolution and sim-
 297 pler parameterization schemes than a state-of-the-art AGCM. A state-of-the-art model
 298 may leave less room for the improvement of the model representation of some dynam-
 299 ical processes. We still believe that the hybrid approach has a great potential to econ-
 300 omically address some of the limitations of even the most sophisticated existing AGCMs.

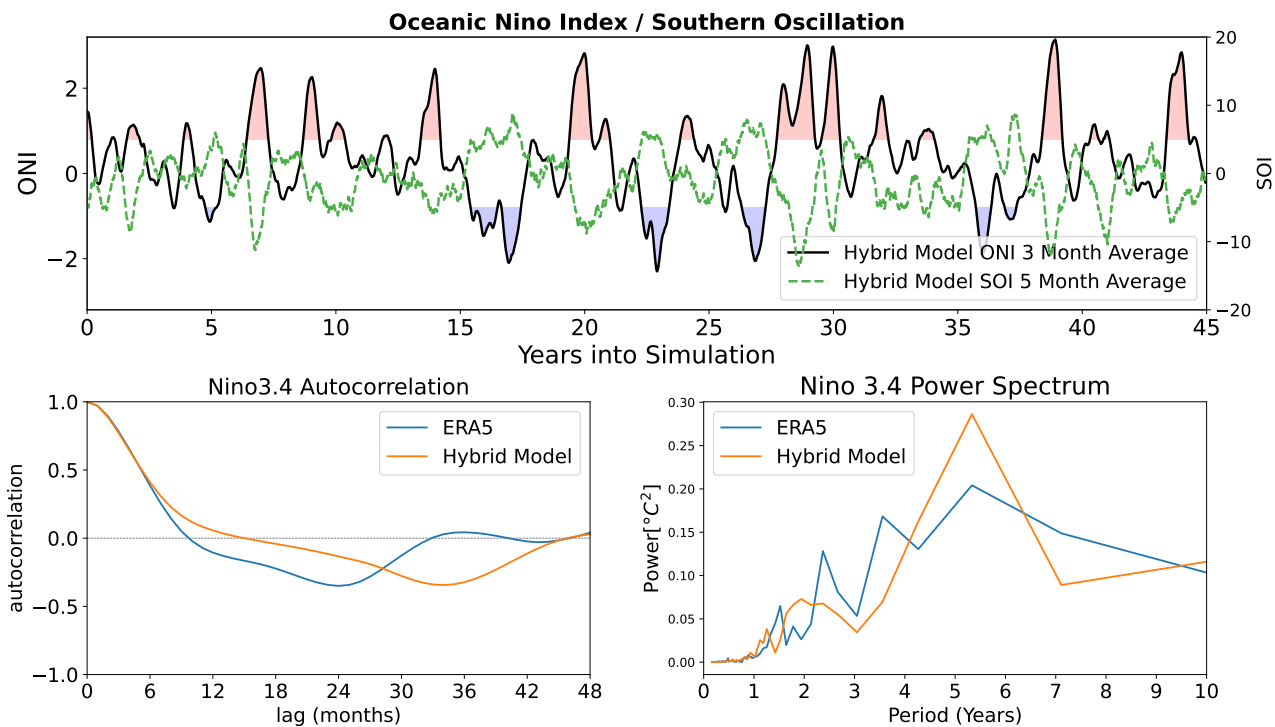


Figure 4. Illustration of the performance of the hybrid model in capturing ENSO. Shown are (top) time series of (solid black) the 3-month running mean of the ONI and (green dashes) the 5-month running mean of the SOI. Red and blue shadings indicate El Niño and La Niña, respectively. Also shown are (bottom left) the autocorrelation functions and (bottom right) power spectra of the Niño 3.4 SST anomalies for (orange) the ERA5 reanalyses and (blue) the coupled model (blue).

301 **Open Research Section**

302 The code to run and analyze the results of the experiments in this study are con-
 303 tained in a GitHub repository <https://github.com/Arcomano1234/SPEEDY-ML> . The
 304 trained weights for the hybrid model used in this study are available online (<https://doi.org/10.5281/zenodo.72228>
 305).

306 **Acknowledgments**

307 This work was supported by DARPA contract HR00112290035, and it was conducted
 308 with the advanced computing resources provided by Texas A&M High Performance Re-
 309 search Computing. Dhruvit Patel provided helpful comments on the manuscript.

310 **References**

311 Andrews, D. G., Holton, J. R., & Leovy, C. B. (1987). Middle atmosphere dynamics.
 312 In (Vol. 40). Academic Press.
 313 Arcomano, T., Szunyogh, I., Pathak, J., Wikner, A., Hunt, B. R., & Ott, E. (2020).
 314 A machine learning-based global atmospheric forecast model. *Geophysical Re-*
 315 *search Letters*, *47*, e2020GL087776.
 316 Arcomano, T., Szunyogh, I., Wikner, A., Pathak, J., Hunt, B. R., & Ott, E. (2022).
 317 A hybrid approach to atmospheric modeling that combines machine learning

- 318 with a physics-based numerical model. *Journal of Advances in Modeling Earth*
 319 *Systems*, 14(3), e2021MS002712. doi: <https://doi.org/10.1029/2021MS002712>
- 320 Brenowitz, N. D., & Bretherton, C. S. (2018). Prognostic validation of a neural net-
 321 work unified physics parameterization. *Geophysical Research Letters*, 45, 6289-
 322 6298.
- 323 Brenowitz, N. D., & Bretherton, C. S. (2019). Spatially extended tests of a neu-
 324 ral network parametrization trained by coarse-graining. *Journal of Advances in*
 325 *Modeling Earth Systems*, 11, 2728-2744.
- 326 Charlton, A. J., & Polvani, L. M. (2007). A new look at stratospheric sudden
 327 warmings. part i: Climatology and modeling benchmarks. *Journal of Climate*,
 328 20(3), 449-469. doi: 10.1175/jcli3996.1
- 329 Chattopadhyay, A., Subel, A., & Hassanzadeh, P. (2020). Data-driven super-
 330 parameterization using deep learning: Experimentation with multiscale lorenz
 331 96 systems and transfer learning. *Journal of Advances in Modeling Earth Sys-*
 332 *tems*, 12(11), e2020MS002084. doi: <https://doi.org/10.1029/2020MS002084>
- 333 Clark, S. K., Brenowitz, N. D., Henn, B., Kwa, A., McGibbon, J., Perkins, W. A.,
 334 ... Harris, L. M. (2022). Correcting a 200 km resolution climate model in
 335 multiple climates by machine learning from 25 km resolution simulations.
 336 *Journal of Advances in Modeling Earth Systems*, 14(9), e2022MS003219. doi:
 337 <https://doi.org/10.1029/2022MS003219>
- 338 Farchi, A., Laloyaux, P., Bonavita, M., & Bocquet, M. (2021). Using machine
 339 learning to correct model error in data assimilation and forecast applications.
 340 *Quarterly Journal of the Royal Meteorological Society*, 147(739), 3067-3084.
 341 doi: <https://doi.org/10.1002/qj.4116>
- 342 Gentine, P., Pritchard, M., Rasp, S., Reinaudi, G., & Yacalis, G. (2018). Could
 343 machine learning break the convection parameterization deadlock? *Geophysical*
 344 *Research Letters*, 45, 5742-5751.
- 345 Hersbach, H., Bell, B., Berrisford, P., Hirahara, S., Horányi, A., Muñoz-Sabater,
 346 J., ... Thépaut, J.-N. (2020). The ERA5 global reanalysis. *Quarterly*
 347 *Journal of the Royal Meteorological Society*, 146(730), 1999-2049. doi:
 348 <https://doi.org/10.1002/qj.3803>
- 349 Jaeger, H. (2001). The “echo state” approach to analysing and training recurrent
 350 neural networks-with an erratum note. *Bonn, Germany: German National Re-*
 351 *search Center for Information Technology GMD Technical Report*, 148.
- 352 Kucharski, F., Molteni, F., & Bracco, A. (2006). Decadal interactions between the
 353 western tropical pacific and the north atlantic oscillation. *Climate Dynamics*,
 354 26(1), 79-91.
- 355 Lukoševičius, M. (2012). A practical guide to applying echo state networks. In
 356 G. Montavon, G. B. Orr, & K.-R. Müller (Eds.), *Neural networks: Tricks of*
 357 *the trade: Second edition* (p. 659-686). Berlin, Heidelberg: Springer Berlin
 358 Heidelberg.
- 359 Lukoševičius, M., & Jaeger, H. (2009). Reservoir computing approaches to recurrent
 360 neural network training. *Computer Science Review*, 3(3), 127-149.
- 361 Menary, M. B., Kuhlbrodt, T., Ridley, J., Andrews, M. B., Dimdore-Miles, O. B.,
 362 Deshayes, J., ... Xavier, P. (2018). Preindustrial control simulations with
 363 hadgem3-gc3.1 for cmip6. *Journal of Advances in Modeling Earth Systems*,
 364 10(12), 3049-3075. doi: <https://doi.org/10.1029/2018MS001495>
- 365 Molteni, F. (2003). Atmospheric simulations using a GCM with simplified phys-
 366 ical parametrizations. I: model climatology and variability in multi-decadal
 367 experiments. *Climate Dynamics*, 20(2), 175-191.
- 368 Pathak, J., Hunt, B., Girvan, M., Lu, Z., & Ott, E. (2018). Model-free prediction
 369 of large spatiotemporally chaotic systems from data: A reservoir computing
 370 approach. *Physical Review Letters*, 120(2), 024102.
- 371 Pathak, J., Wikner, A., Fussell, R., Chandra, S., Hunt, B. R., Girvan, M., & Ott,
 372 E. (2018). Hybrid forecasting of chaotic processes: Using machine learning in

- 373 conjunction with a knowledge-based model. *Chaos*, 28(4), 041101.
- 374 Rasp, S., Pritchard, M. S., & Gentile, P. (2018). Deep learning to represent subgrid
375 processes in climate models. *Proceedings of the National Academy of Sciences*,
376 115, 9684-9689.
- 377 Walleshauser, B., & Bollt, E. (2022). Predicting sea surface temperatures with cou-
378 pled reservoir computers. *Nonlin. Processes Geophys.*, 29(3), 255-264. doi: 10
379 .5194/npg-29-255-2022
- 380 Watt-Meyer, O., Brenowitz, N. D., Clark, S. K., Henn, B., Kwa, A., McGibbon,
381 J., ... Bretherton, C. S. (2021). Correcting weather and climate models by
382 machine learning nudged historical simulations. *Geophysical Research Letters*,
383 48(15), e2021GL092555. doi: <https://doi.org/10.1029/2021GL092555>
- 384 Wikner, A., Pathak, J., Hunt, B., Girvan, M., Arcomano, T., Szunyogh, I., ... Ott,
385 E. (2020). Combining machine learning with knowledge-based modeling for
386 scalable forecasting and subgrid-scale closure of large, complex, spatiotemporal
387 systems. *Chaos*, 30(5), 053111.
- 388 Zhang, G. J., Song, X., & Wang, Y. (2019). The double ITCZ syndrome in
389 GCMs: A coupled feedback problem among convection, clouds, atmo-
390 spheric and ocean circulations. *Atmospheric Research*, 229, 255-268. doi:
391 <https://doi.org/10.1016/j.atmosres.2019.06.023>